Effective and accurate representation of extended Bloch states on finite Hilbert spaces

Luis A. Agapito,[1,2,*] Andrea Ferretti,[3] Arrigo Calzolari,[1,3] Stefano Curtarolo,[2,4] and Marco Buongiorno Nardelli[1,2,†]

[1]*Department of Physics, University of North Texas, Denton, Texas 76203, USA*

[2]*Center for Materials Genomics, Duke University, Durham, North Carolina 27708, USA*

[3]*CNR-NANO S3 Center, Istituto Nanoscienze, I-41125 Modena, Italy*

[4]*Department of Mechanical Engineering and Materials Science, Duke University, Durham, North Carolina 27708, USA*

(Received 24 June 2013; published 21 October 2013)

We present a straightforward, noniterative projection scheme that can represent the electronic ground state of a periodic system on a finite atomic-orbital-like basis, up to a predictable number of electronic states and with controllable accuracy. By cofiltering the projections of plane-wave Bloch states with high-kinetic-energy components, the richness of the finite space and thus the number of exactly-reproduced bands can be selectively increased at a negligible computational cost, an essential requirement for the design of efficient algorithms for electronic structure simulations of realistic material systems and massive high-throughput investigations.

DOI: 10.1103/PhysRevB.88.165127 PACS number(s): 71.15.Ap, 71.23.An, 73.23.Ad

I. INTRODUCTION

The electronic structure of solids is commonly described using plane-wave (PW) basis functions, which represent naturally the Fourier algebra of periodic systems and whose completeness is easily improvable up to any desirable accuracy. However, their delocalized character is often not appropriate for the description of highly localized electronic systems unless a very large number of basis functions is used. For these reasons, the development of minimal-space solutions such as atomic-orbital (AO) Bloch sums, capable of capturing with satisfactory accuracy the properties of solids and molecules on finite Hilbert spaces, has been central to methodological developments in quantum chemistry and solid-state physics since the 1970s.[1,2]

AO representations are desirable not only for computational accuracy and finiteness of the basis set, but also to gain a better chemical interpretation of the quantum-mechanical wave function. They are essential in a gamut of applications such as the construction of model Hamiltonians for correlated electrons and magnetic systems; dynamical mean-field theory;[3] evaluation of quantum transport properties;[4] design of semiempirical potentials for solids[5] and biomolecules;[6] calculation of exact-exchange integrals; and applications within linear scaling of density-functional theory[7] and coupled-cluster,[8] quantum Monte Carlo,[9] and *GW*[10] methods. More generally, localized-space representations are increasingly in demand as novel materials with stronger electron localization and correlation are vigorously sought for their rich physical and chemical properties.[11] Moreover, they allow the calculation of the electronic states of materials on ultradense **k**-space grids for accurate Brillouin-zone (BZ) integrations, an essential requirement for the high-throughput computational materials applications central to the mission of the Materials Genome Initiative.[11,12]

In the last decade, formidable efforts towards this goal have resulted in a variety of methodologies using, for instance, muffin-tin orbitals of arbitrary order (*N*MTO)[13] or maximally localized Wannier functions (MLWFs)[14] to construct minimal Hilbert spaces. The MLWF method stands as the norm for maximal localization of the real-space basis starting from pseudo-potential PW calculations; however, it is not straightforward either to decide the appropriate number of target PW bands (energy range) to match, and thus the size of the Hilbert space, or to achieve convergence for systems with diffused electrons.

On the other hand, noniterative methods such as *direct projection* (Ref. 14, Sec. II.i.1), QUAMBO,[15] and QO,[16] which do not seek an iterative construction of the finite Hilbert space but rely on an AO basis provided as input, are a good compromise between speed (noniterative postprocessing) and accurate reproduction of the occupied energy bands while maintaining AO similarity.

While the primary goal of these methods is to construct real-space wave functions with high localization, reciprocal-space Hamiltonians matrices can be built using these wave functions as well. The resulting band structure can exactly reproduce unentangled bands (bundles of bands that do not overlap others in energy across the BZ and are, therefore, isolated by energy gaps), e.g., the occupied manifold of an insulator or a semiconductor like silicon [black curves in Fig. 1(a)]. In general, however, the bands in metals (or the unoccupied manifold in semiconductors) are entangled. While the iterative MLWF method can further enforce reproduction of those bands inside a frozen energy window via a disentanglement procedure,[17] adding an extra layer of computational complexity, the noniterative methods fail to systematically reproduce those bundles, especially the upper unoccupied states [circles in Fig. 1(a)].

In this article, we present a fast, noniterative procedure that effectively and accurately reproduces a predictable number of eigenenergies (bands) regardless of entanglement. The antibonding fraction of the wave function, scattered through the quasi-infinite unoccupied subspace of the PW approach, is efficiently mapped into the finite-space Hamiltonian through straightforward matrix operations of projections on controlled basis and sequential filtering to automatically discard all unphysical solutions.

II. METHODOLOGY

A. Linear-combination-of-AOs (LCAO) representation of Bloch states

For simplicity, in this work we use the finite Hilbert spaces defined by the set of pseudo–atomic orbitals (PAOs) $\phi(\mathbf{r})$,

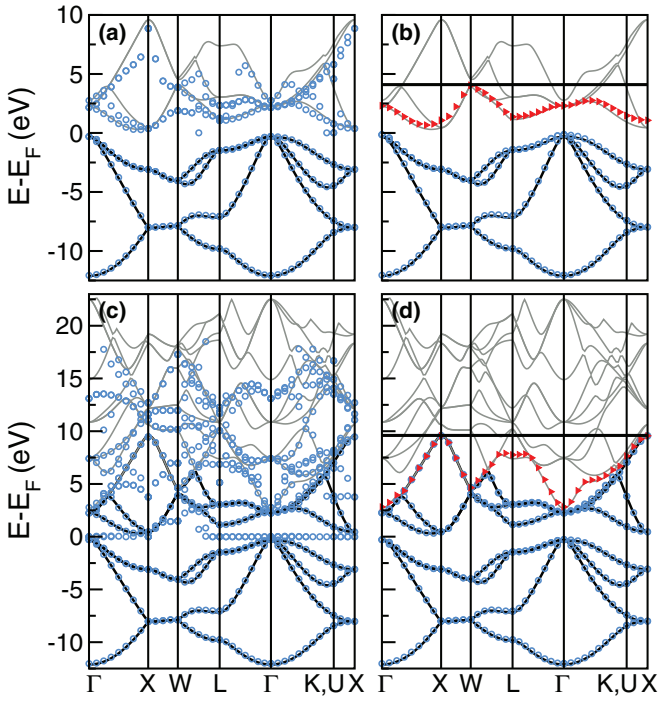

FIG. 1. (Color online) Si band structures from projected LCAO Hamiltonian matrices $H^{\mathbf{k}}(\kappa,N)$. Eigenenergies are represented by circles, triangles, or horizontal solid lines (flat bands). The electronic structure is expanded in an *sp* (a,b) and an *spd* (c,d) finite space. (a,c) Direct-projection scheme (no filtering, $N = M$; no shifting, $\kappa = 0$). (b,d) Filtered + shifted projections. Degenerate flat bands (3- and 10-fold) are rigidly shifted by κ (4.1 and 9.6 eV) and plotted as horizontal solid lines. Reference PW bands are shown in black ($\mathcal{P}_n \geqslant 0.9$) or gray ($\mathcal{P}_n < 0.9$).

employed in the generation of atomic pseudopotentials. While the richness of the PAO basis can be systematically increased by including more radial functions and angular momentum projectors in the construction of pseudo–wave functions, we stress that this is just a choice of convenience. Our procedure is completely general and can be applied to any finite basis, including polarized and diffused Gaussian sets, thus providing a direct bridge between the language of solid-state physics and that of theoretical quantum chemistry.

As the first example we choose silicon (see Fig. 1), where we have used an *sp* (minimal) basis set to construct the Bloch sums, $\phi_{\mu\mathbf{k}}(\mathbf{r}) = \frac{1}{N_\mathcal{V}} \sum_{\mathbf{R}} e^{-i\mathbf{k}\cdot\mathbf{R}} \phi_\mu(\mathbf{r}-\mathbf{R})$, that span the finite Hilbert space Ω_1.[18] These Bloch sums can be seen as the discrete Fourier transform of the corresponding PAO $\phi_\mu(\mathbf{r})$ replicated on a periodic box containing $N_\mathcal{V}$ lattice vectors $\mathbf{R}$ and, thus, the same number of $\mathbf{k}$ vectors in the BZ. The starting PW Bloch states $|\psi^{\mathrm{PW}}_{n\mathbf{k}}\rangle$ are obtained using the QUANTUM ESPRESSO packages.[19] For convenience, let us switch to a Löwdin-orthogonalized basis representation $\bar{\phi}_{\mu\mathbf{k}} = \sum_\nu (S^{\mathbf{k}^{-\frac{1}{2}}})_{\mu\nu} \phi_{\nu\mathbf{k}}$, where $S^{\mathbf{k}}_{\mu\nu} = \langle\phi_{\mu\mathbf{k}}|\phi_{\nu\mathbf{k}}\rangle$ are the overlap matrices. The PW states are projected onto the finite Hilbert space of the PAOs via the operator $\hat{P}^{\mathbf{k}} = \sum_\mu |\bar{\phi}_{\mu\mathbf{k}}\rangle\langle\bar{\phi}_{\mu\mathbf{k}}|$. Then $|\psi_{n\mathbf{k}}\rangle = \sum_\mu a^{\mathbf{k}}_{\mu n} |\bar{\phi}_{\mu\mathbf{k}}\rangle$, with expansion coefficients

$$a^{\mathbf{k}}_{\mu n} = \langle \bar{\phi}_{\mu\mathbf{k}} | \psi^{\mathrm{PW}}_{n\mathbf{k}} \rangle.$$

Similar expansions are used in the LCAO solution of the Kohn-Sham equation,[20] where the Hamiltonian is

$$\mathcal{H}^{\mathbf{k}} = A^{\mathbf{k}} E^{\mathbf{k}} A^{\mathbf{k}\dagger} \tag{1}$$

and the matrices $A^{\mathbf{k}}$ of the expansion coefficients are found self-consistently under the orthonormality constraint $A^{\mathbf{k}\dagger} A^{\mathbf{k}} = I$. Here $A^{\mathbf{k}}$ is built columnwise from the projection coefficients $a^{\mathbf{k}}_{\mu\nu}$; each column represents the LCAO wave function $|\psi_{n\mathbf{k}}\rangle$ for a given band n. $\mathcal{H}^{\mathbf{k}}$ and $A^{\mathbf{k}}$ are of dimensions $M \times M$ and $M \times N$, respectively. M is the size of the Hilbert space and N is the number of PW bands selected for projection. $E^{\mathbf{k}}$ is an $N \times N$ diagonal matrix of the N lowest PW eigenvalues, $E^{\mathbf{k}} = \mathrm{diag}(\epsilon^{\mathrm{PW}}_1, \epsilon^{\mathrm{PW}}_2, \ldots, \epsilon^{\mathrm{PW}}_N)$.

B. Band projectability

Going back to the example of Si in space Ω_1 ($M = 8$) in Fig. 1(a), its corresponding LCAO Hamiltonian $\mathcal{H}^{\mathbf{k}}$ yields a manifold of eight bands (represented by circles), some of which, especially in the unoccupied energy region, noticeably deviate from the reference PW bands (gray lines). This stems from the less than perfect projectability of those unoccupied PW states onto the inherently incomplete finite space. In turn, low projectability breaks the unitary constraint of the LCAO method, $A^{\mathbf{k}} A^{\mathbf{k}\dagger} \neq 1$. To quantify this effect, we define a projectability number $\mathcal{P}_n = \min\{\sum_\mu a^{\mathbf{k}*}_{\mu n} a^{\mathbf{k}}_{\mu n}, \forall \mathbf{k} \in \mathrm{BZ}\}$ as an *a priori* test for the representability of each PW band. The closer $\mathcal{P}_n$ is to 1, the better the fidelity of the corresponding LCAO band. Numerical values of $\mathcal{P}_n$ for the systems studied here are summarized in Table I. We set an arbitrary cutoff of 0.9 as the condition for exact representability so that, with the minimal space Ω_1, we can expect exact representability only for the lowest $N = 4$ PW bands [the complete occupied manifold; black lines in Fig. 1(a)], with deviations less than 57.2 meV. A richer space, Ω_2 ($M = 18$),[18] which includes *d* functions, yields $\mathcal{P}_7 \geqslant 0.9$ and should therefore support exact representation of the electronic structure up to $N = 7$ PW bands [black lines in Fig. 1(c)], which includes 3 unoccupied bands. However, the apparently bad reproducibility of the electronic structure in the energy window 0–10 eV shown in Fig. 1(c) seems to suggest otherwise.

The progressive loss of representability of the top unoccupied PW bands mentioned above is a common issue even

TABLE I. Projectability ($\mathcal{P}_n$) and BZ rms average of $\Delta\epsilon_n$ (in eV) per band n of $H^{\mathbf{k}}(\kappa,N)$. $\kappa = 0$, 9.6, and 10 eV and $N = 5$, 8, and 13 for Si Ω_1, Si Ω_2, and Mo Ω_3, respectively

	Si Ω_1		Si Ω_2			Mo Ω_3[a]	
n	$\mathcal{P}_n$	rms	$\mathcal{P}_n$	rms	n	$\mathcal{P}_n$	rms
1	0.9927	0.0478	0.9953	0.0792	5	0.9979	0.0140
2	0.9622	0.0572	0.9933	0.0555	6	0.9937	0.0183
3	0.9622	0.0252	0.9952	0.0382	7	0.9873	0.0386
4	0.9622	0.0203	0.9967	0.0266	8	0.9924	0.0275
5	0.4755	1.9200	0.9934	0.0267	9	0.9905	0.0302
6	0.0660		0.9771	0.0316	10	0.9286	0.0602
7	0.0941		0.9728	0.0380	11	0.0000	3.5975
8	0.0652		0.8464	0.1382	12	0.0000	3.3524

[a]The four semicore bands have exact projectability.

for more sophisticated noniterative and iterative approaches, and not at all limited to the LCAO bands obtained as first-order solutions via the *direct-projection* scheme. The following is nonetheless observed: (i) The overall matching to the lower unoccupied bands significantly improves with the richer space Ω_2 compared to Ω_1 (cf. circles on solid lines for the first unoccupied band along the Γ-K path and along Γ-X for the second and third such bands). (ii) Unoccupied states increasingly exhibit high-kinetic-energy PW components, which do not project well on localized basis. The low projectability of the upper PW states yields low values of the $a^{\mathbf{k}}_{mn}$ coefficients. Consequently, the corresponding LCAO eigenstates consistently default to regions of lower energy and yield the apparent overall poor reproducibility shown in Fig. 1(c). (iii) Singular values are introduced in the Hamiltonian in the case of no projectability, thus the observed zero-energy LCAO eigenvalues.

C. Band filtering and shifting

In order to resolve points (ii) and (iii), we filter out PW states with low projectability by choosing all the PW bands that satisfy $\mathcal{P}_n \geqslant 0.9$. The number of these PW bands, N, determines the number of columns in the matrix $A^{\mathbf{k}}$, which is generally not square and nonunitary.

In the formulation of the LCAO Hamiltonian we can always define a square $M \times M$ matrix $[A^{\mathbf{k}}\mathbf{0}]$, which extends $A^{\mathbf{k}}$ with $M - N$ columns of zeros, and fill $E^{\mathbf{k}}$ with the same number of zero eigenvalues. Then Eq. (1), can be more generally written as a product of square matrices:

$$\mathcal{H}^{\mathbf{k}} = [A^{\mathbf{k}}\mathbf{0}]\mathrm{diag}\big(\epsilon_1^{\mathrm{PW}},\ldots,\epsilon_N^{\mathrm{PW}},0,\ldots,0\big)[A^{\mathbf{k}}\mathbf{0}]^{\dagger}. \qquad (2)$$

Since the product $[A^{\mathbf{k}}\mathbf{0}][A^{\mathbf{k}}\mathbf{0}]^{\dagger}$ is not unitary, the spectrum of its eigenvalues will contain the first N eigenvalues of $A^{\mathbf{k}}A^{\mathbf{k}\dagger}$, of the form $\lambda_n = 1 - \delta_n$, with $0 \leqslant \delta_n \leqslant 0.1$ guaranteed by the projectability criterion adopted. The remaining $M - N$ eigenvalues will all be zero.

Using the canonical representation, $[A^{\mathbf{k}}\mathbf{0}][A^{\mathbf{k}}\mathbf{0}]^{\dagger} = UDU^{\dagger}$ we can write $[A^{\mathbf{k}}\mathbf{0}] = UD^{\frac{1}{2}}$, where $D = \mathrm{diag}(\lambda_1,\ldots,\lambda_N,\lambda_{N+1},\ldots,\lambda_M)$, and rewrite Eq. (2) as

$$\mathcal{H}^{\mathbf{k}} = U\mathrm{diag}\big(\epsilon_1^{\mathrm{PW}}(1-\delta_1),\ldots,\epsilon_N^{\mathrm{PW}}(1-\delta_N),0,\ldots,0\big)U^{\dagger}.$$

This expression explicitly shows that having a nonunitary space $A^{\mathbf{k}}$ applies a multiplicative factor to each PW eigenvalue. Filtering the low-projectability bands is a necessary step to guarantee that these corrections are minimal. The $M - N$ null eigenvalues appear as degenerate "flat" bands at zero energy and need to be selectively moved out of the energy window of interest. To do so we introduce the "shifting" operator,

$$\mathcal{I}^{\mathbf{k}} = I - A^{\mathbf{k}}A^{\mathbf{k}\dagger} = U\mathrm{diag}(\delta_1,\ldots,\delta_N,1,\ldots,1)U^{\dagger},$$

and rewrite the Hamiltonian as

$$H^{\mathbf{k}}(\kappa,N) = \mathcal{H}^{\mathbf{k}} + \kappa\mathcal{I}^{\mathbf{k}} = U\mathrm{diag}(\bar{\epsilon}_1,\ldots,\bar{\epsilon}_N,\kappa,\ldots,\kappa)U^{\dagger}. \qquad (3)$$

Equation (3) is the central result of our work. The $\mathcal{I}^{\mathbf{k}}$ operator allows a selective shifting, by κ, of the $M - N$ flat bands with negligible effect on the other N high-projectability bands, with eigenenergy deviations $\Delta\epsilon_n \leqslant (1 - \mathcal{P}_n)(\kappa - \epsilon_n^{\mathrm{PW}})$. The last factor is interpreted as the energy window between the highest band under consideration (Nth) of energy $\sim\kappa$ and a given PW eigenvalue, and it is maximal for the lowest band $n = 1$. In practice, since the upper limit of the energy window is usually only ~2–5 eV above E_f, the correction can be made arbitrarily small by appropriate choice of the projectability number $\mathcal{P}_n$.

The LCAO band structures (circles and triangles) in Figs. 1(b) and 1(d) showcase the dramatic improvement, with respect to Figs. 1(a) and 1(c), which is achieved by filtering and shifting the low-projectability bands. It confirms the exact reproducibility of four and seven bands (circles) expected for the two different spaces, respectively. For further illustration, we included the projections of an additional PW band (with $\mathcal{P}_n < 0.9$) in building the Hamiltonians. As expected, this LCAO band [fifth in Fig. 1(b) and eighth in Fig. 1(d), represented by triangles] does not *exactly* reproduce the PW reference. Nonetheless, the band closely follows the reference across the BZ, except at X and U-X in Fig. 1(b) and L in Fig. 1(d), which are the BZ regions where the projectability is the lowest. The eighth band shows an overall good fidelity, consistent with the relatively high projectability, $\mathcal{P}_8 = 0.8335$.

To demonstrate the performance of our procedure in the case of entangled bands, we computed the band structure of an intrinsically delocalized metallic system such as molybdenum bcc (Fig. 2; Ω_3, $M = 13$)[18] and of a gold nanowire (Fig. 4; Ω_4, $M = 90$).[18] As observed in the silicon case, in both metallic systems the low-projectability states can default

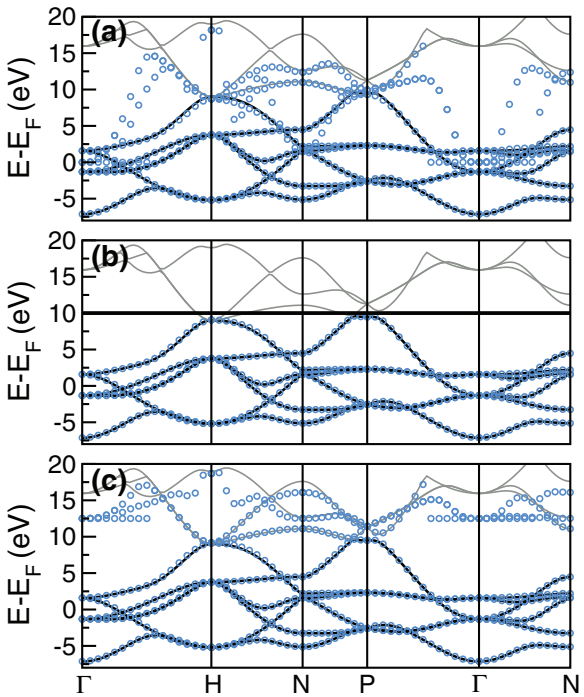

FIG. 2. (Color online) Band structure of Mo bcc under space Ω_3. (a) Direct-projection scheme ($N = 13$, $\kappa = 0$ eV). (b) Filtered + shifted projection ($N = 7$, $\kappa = 10$ eV). (c) Unfiltered + shifted projection ($N = M = 13$, $\kappa = 12.5$ eV). The eigenenergies of the LCAO Hamiltonian $H^{\mathbf{k}}(\kappa,N)$ are represented by circles. PW bands of high ($\mathcal{P}_n \geqslant 0.9$) projectability are shown by solid black lines; those of low ($\mathcal{P}_n < 0.9$) projectability, by solid gray lines. The four low-lying semicore bands ($4s4p$) are not shown.

to the bottom of the unoccupied energy region, as in the direct-projection band structure in Fig. 2(a) for Mo. The effect of the low-projectability states is more detrimental in the nanowire case, where they hybridize with states of otherwise high fidelity and any resemblance to the PW reference is lost [Fig. 4(a)].

For Mo, the space Ω_3 supports the exact representation of up to six PW bands (beyond the four semicore bands; not shown), as listed in Table I for $\mathcal{P}_n \geqslant 0.9$. The band structure from the filtered + shifted scheme [Fig. 2(b)] confirms the reproducibility of all these PW bands with root-mean-square (rms) deviations of less than 60.2 meV even for the large value of κ (10 eV) used here.

In particular cases it may be advantageous to keep the low-projectability PW states as in the direct-projection scheme; for instance, the low-projectability PW bands $n = 11$ and 12 of Mo bcc exhibit local high projectability around H and P. Applying a κ shift to the direct-projection Hamiltonian, i.e., $H^{\mathbf{k}}(12.5, M)$, yields an expanded range of band-structure reproducibility, up to 12.5 eV [Fig. 2(c)], which is directly due to the inclusion of bands 11 and 12.

III. APPLICATIONS OF LCAO HAMILTONIANS

A. Band interpolation

Once the LCAO matrices $H^{\mathbf{k}}(\kappa, N)$ are known, one can directly construct the real-space localized Hamiltonian as

$$H^{\mathbf{0R}} = \frac{1}{N_{\mathcal{V}}} \sum_{\mathbf{k}} e^{-i\mathbf{k}\cdot\mathbf{R}} H^{\mathbf{k}}(\kappa, N). \tag{4}$$

Conversely, these local matrices allow us to obtain the *interpolated* band structure at any arbitrary **k** vector,[21,22] with the same accuracy defined by the projectability number, by diagonalizing the interpolated reciprocal-space Hamiltonian,

$$H^{\mathbf{k},\text{interpolated}} = \sum_{\mathbf{R}} e^{i\mathbf{k}\cdot\mathbf{R}} H^{\mathbf{0R}}.$$

B. Band decomposition and Fermi surface analysis

A valuable application of this procedure is in the evaluation of fundamental physical properties of materials that require an accurate representation of the electronic states across the whole BZ. A typical example is the calculation of the Fermi surface of any metal, which typically requires extraordinary computational efforts. Within our approach the Fermi surface is straightforwardly obtained by the direct evaluation of the interpolated band structure of the system via the real-space Hamiltonians. The Fermi energy of Mo bcc is crossed at various **k** points in the three-dimensional BZ. The collection of all such points defines its Fermi surface, which is shown in Fig. 3(e). Furthermore, it is determined that the crossing states can have three distinct atomic characters. Bands of different character are indicated by circles of different colors at the crossing of the Fermi level (horizontal dashed line) in Fig. 3(a). The decomposition of the Fermi surface based on the atomic character of the crossing states is shown in Figs. 3(b)–3(d).

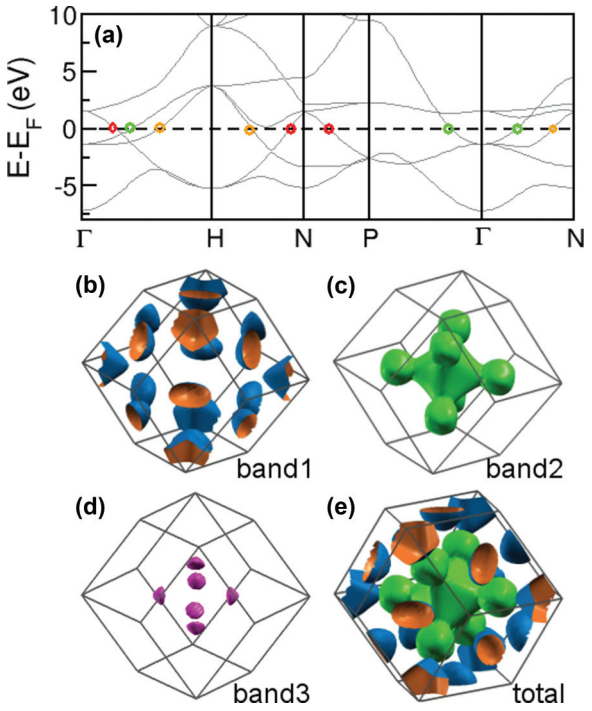

FIG. 3. (Color online) Fermi surface of Mo bcc bulk. (a) Colored circles identify the same band crossing the Fermi energy (horizontal dashed line). Orange, band 1; green, band 2; red, band 3. (b–d) Individual-band contributions to the Fermi surface. (e) Total Fermi surface.

C. Electrical conductance

Another straightforward application of LCAO Hamiltonians is the calculation of the electrical conductance through a nanowire. Our procedure reduces the problem of calculating electron transport[4,21] to the computationally inexpensive postprocess of evaluating Eq. (A6). We choose a gold nanowire[23] as a prototypical example. Bands obtained from the direct-projection scheme are shown in Fig. 4(a). Unphysical

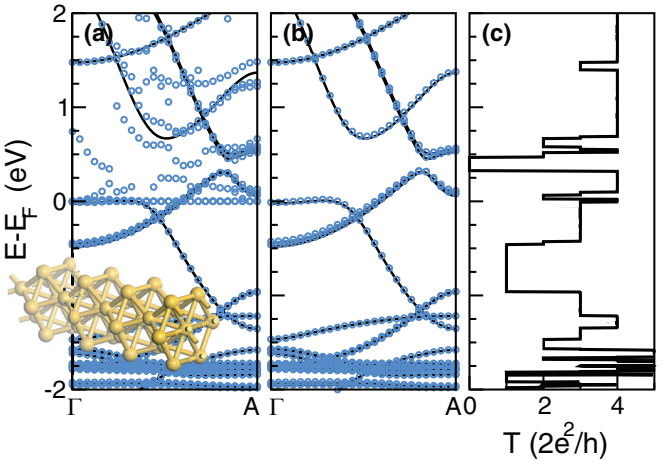

FIG. 4. (Color online) Band structure and quantum transmittance spectrum of a gold nanowire. (a) Direct-projection and (b) filtered + shifted ($N = 62, \kappa = 3$ eV) band structures are represented by circles; PW bands, by solid lines. (c) Quantized transmittance of the nanowire.

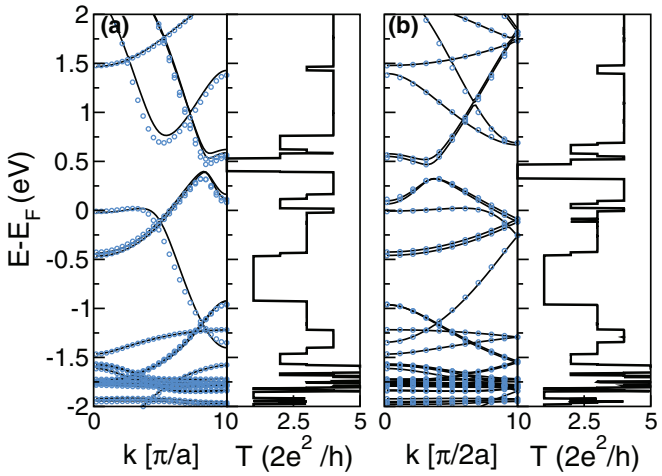

FIG. 5. (Color online) Effect of the nearest principal-layer approximation on the interpolated band structure (left) and quantized conductance (right). The principal layer is approximated with (a) one and (b) two unit cells (=4.71 Å). The (blue) circles are the eigenvalues of $H^{\mathbf{k}}$ and the underlying solid lines are the corresponding interpolated bands.

zero-energy eigenstates, discussed in Sec. II C, cover the entirety of the BZ. They are removed by applying a shifting of $\kappa = 3$ eV to the filtered bands (lowest $N = 62$ bands) and the resulting LCAO eigenstates are represented by blue circles in Fig. 4(b). The LCAO real-space Hamiltonians $H^{\mathbf{00}}$ and $H^{\mathbf{01}}$ are obtained according to Eq. (4) and the electrical transmittance $T(E)$, in Fig. 4(c), is computed from these matrices as described in the Appendix.

Furthermore, formulating the LCAO Hamiltonian $H^{\mathbf{k}}$ directly in reciprocal space allows the discrimination of the two most common sources of error in electronic transport simulations: (i) the incompleteness of the finite space, which is reflected in the mismatch between the PW and the LCAO band structures [cf. Fig. 5(b)] and can be made arbitrarily small by our procedure; and (ii) the real-space interaction truncation in the choice of the principal layer. The latter is outside the scope of any reciprocal-space mapping procedure $\psi^{\mathrm{PW}}_{n\mathbf{k}} \rightarrow \psi^{\mathrm{LCAO}}_{n\mathbf{k}}$. Nonetheless, such error is introduced when formulating real-space local Hamiltonians $H^{\mathbf{0R}}$ [via Eq. (4)]. This real-space truncation error is reflected in the mismatch between the interpolated band structure (solid lines) and the LCAO eigenvalues [(blue) circles] shown in Fig. 5(a) and can be systematically reduced by increasing the size of the principal layer. For instance, the mismatch is eliminated when doubling the size of the nanowire principal layer (to a lattice constant of 2×4.71 Å), as shown in Fig. 5(b).

The three applications shown here are implemented in the GPL open-software packages WANT and QUANTUM ESPRESSO of Refs. 4 and 19, respectively.

IV. CONCLUSIONS

These results have far-reaching implications, well beyond the practical applications shown here. In fact, our method allows control of the size (richness) of the finite Hilbert space of the basis functions, an archetypal feature in quantum chemistry, which in turns provides flexibility to converge to the true infinite-space solution in the limit of infinite PWs.[24] Expanding the space increases the number of unoccupied bands with the concomitant bad reproducibility problem that challenges current methodologies and has biased solutions toward minimal basis, which only bypasses the problem by reducing the number of unoccupied bands.

Contrarily to the spirit of the *N*MTO and MLWF methods, our technique does not seek the construction of (heavily customized, localized) basis functions. Its importance resides in allowing noniterative reproduction a large number of energy bands using standard quantum-chemistry basis sets or equivalent. In that regard, the present methodology completely supersedes the need for engineered basis functions such as MLWFs or *N*MTOs.

The central result of this article, Eq. (3), allows us to obtain an exact representation of all the PW bands that complies with our high projectability criterion in a procedure of negligible computational cost, opening the way to the design of efficient algorithms for electronic structure simulations of realistic material systems, within the high-throughput materials framework.[25]

ACKNOWLEDGMENTS

This work was supported, in part, by SRC through Task ID P14924 at the Center for Electronic Materials Processing and Integration, University of North Texas, ONR-MURI N000141310635, and by the Center for Materials Genomics, Duke University.

APPENDIX: ELECTRICAL CONDUCTANCE IN PERIODIC NANOWIRES

The set of real-space Hamiltonian $H^{\mathbf{0R}}$ and overlap matrices $S^{\mathbf{0R}}$, in the general case of a nonorthogonal basis, contain the necessary information to compute the electronic properties along the nanowire. In the site representation, the spatial coordinate $\mathbf{r}$ of the wave function is discretized to lattice vector $\mathbf{R}$, thus, each periodic cell is considered an abstract single site $\mathbf{R}$.

Following the translational Bloch theorem, a wave function $\psi^{\mathbf{k}} \equiv \psi^{\mathbf{k}}_{\mathbf{0}}$ evaluated at a generic site $\mathbf{r} = \mathbf{0}$ relates to the next site, $\mathbf{r} = -\mathbf{1}$ or $\mathbf{1}$, by a phase factor, that is, $\psi^{\mathbf{k}}_{-\mathbf{1}} = e^{-i\theta}\psi^{\mathbf{k}}_{\mathbf{0}}$ and $\psi^{\mathbf{k}}_{\mathbf{1}} = e^{i\theta}\psi^{\mathbf{k}}_{\mathbf{0}}$, where $\theta = \mathbf{k}\cdot\mathbf{1}$. In a nonorthogonal LCAO space, the wave function satisfies the Roothaan equation,

$$H^{\mathbf{k}}\psi^{\mathbf{k}} = E^{\pm}S^{\mathbf{k}}\psi^{\mathbf{k}}. \tag{A1}$$

Both Hamiltonian and overlap matrices are obtained from the Fourier transform or the corresponding real-space quantities:

$$H^{\mathbf{k}} = \sum_{\mathbf{R}=-\mathbf{1},\mathbf{0},\mathbf{1}} e^{i\mathbf{k}\cdot\mathbf{R}} H^{\mathbf{0R}},$$

$$S^{\mathbf{k}} = \sum_{\mathbf{R}=-\mathbf{1},\mathbf{0},\mathbf{1}} e^{i\mathbf{k}\cdot\mathbf{R}} S^{\mathbf{0R}}.$$

The truncation in the Fourier transform corresponds to the principal-layer approximation. A principal layer is composed of one or more primitive cells, such that interactions beyond nearest principal layers are made negligible. Then Eq. (A1)

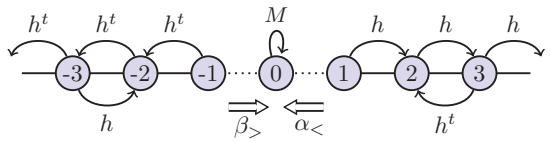

FIG. 6. (Color online) Schematic representation of the quadratic eigenvalue equations (A2) and (A3) as a one-dimensional tight-binding model.

becomes

$$[M\lambda - h - h^t\lambda^2]\psi^{\mathbf{k}}_{\mathbf{1}} = 0 \tag{A2}$$

or, equivalently,

$$[M\lambda^{-1} - h^t - h\lambda^{-2}]\psi^{\mathbf{k}}_{-\mathbf{1}} = 0, \tag{A3}$$

with $\lambda = e^{-i\theta}$, $M^{\pm} = E^{\pm}S^{\mathbf{00}} - H^{\mathbf{00}}$, $h^{\pm} = H^{\mathbf{01}} - E^{\pm}S^{\mathbf{01}}$, and the definition $h^t(E) \equiv h^{\dagger}(E^*)$. It assumes Hermitian matrices, i.e., $H^{\mathbf{0},-\mathbf{1}} = (H^{\mathbf{01}})^{\dagger}$.

Equations (A2) and (A3) are standard quadratic eigenvalue problems of the form $a_2\lambda^2 + a_1\lambda + a_0 = 0$. The solutions λ_n represent all the propagating modes of the nanowire. Solutions with $|\lambda_n| > 1$ are evanescent modes decaying (traveling) to the right, while $|\lambda_n| < 1$ are evanescent modes traveling to the left. Modes with $|\lambda_n| = 1$ are standing waves, i.e., Bloch states. An infinitesimal imaginary quantity η is added to the energy, thus the definition $E^{\pm} = E \pm i\eta$. In this way the phase factors are moved slightly away from the unitary circle and an unambiguous traveling direction can be assigned.

As a result, half of the $2M$ solutions of the quadratic equation are discerned as left-traveling and the other as right-traveling, denoted by the subscripts $<$ and $>$, respectively. Compounding all the left-traveling eigenvalues $\lambda_{n<}$ and eigenvectors $\psi^{\mathbf{k}}_{\mathbf{1}n<}$ into the $M \times M$ matrices $\Lambda_<$ and $U_{1,<}$, respectively, the matrix $\alpha_<$ is defined as

$$\alpha_< = U_{1,<}\Lambda_<(U_{1,<})^{-1}, \tag{A4}$$

which satisfies Eq. (A2), i.e., $M\alpha - h - h^t\alpha^2 = 0$.

Physically, it represents the propagating modes of a semi-infinite right wire (starting at site **1**) leaking into site **0**, as shown schematically in Fig. 6. Analogously, the effect of all right-moving modes of a semi-infinite left wire (which starts at site $-\mathbf{1}$) on site **0** is given by the solutions of Eq. (A3). The matrix $\beta_>$ that satisfies that equation is

$$\beta_> = U_{-1,>}\,(\Lambda_>)^{-1}\,(U_{-1,>})^{-1}. \tag{A5}$$

The use of h and h^t is inverted in Eq. (A3) with respect to Eq. (A2). This effectively flips the wave vector of the modes, i.e., $\lambda \leftarrow \lambda^{-1} = \lambda^*$, and is accounted by taking the inverse of Λ in Eq. (A5).

Finally, in the case of an infinite nanowire, all relevant electronic properties such as the Green's function G and the electrical conductance T are directly obtained from $\alpha_<$ and $\beta_>$ using the following:

$$\begin{aligned}
\Sigma^{\pm}_L &= (h^{\mp})^{\dagger}\alpha^{\pm}_<, \quad \Sigma^{\pm}_R = (h^{\pm})\beta^{\pm}_>, \\
\Gamma_{L/R} &= i\left(\Sigma^{+}_{L/R} - \Sigma^{-}_{L/R}\right), \\
G^{\pm} &= (h^{\pm}[(\alpha^{\pm}_<)^{-1} - \beta^{\pm}_>])^{-1}, \\
T(E) &= \mathrm{trace}[\Gamma_L G^{+}\Gamma_R G^{-}].
\end{aligned} \tag{A6}$$

*luis.agapito@gmail.com
†mbn@unt.edu

[1] D. J. Chadi, Phys. Rev. B **16**, 3572 (1977).
[2] D. Sánchez-Portal, E. Artacho, and J. M. Soler, Solid State Commun. **95**, 685 (1995).
[3] F. Lechermann, A. Georges, A. Poteryaev, S. Biermann, M. Posternak, A. Yamasaki, and O. K. Andersen, Phys. Rev. B **74**, 125120 (2006).
[4] WANT code by A. Ferretti, L. Agapito, A. Calzolari, and M. Buongiorno Nardelli, http://www.wannier-transport.org; A. Calzolari, N. Marzari, I. Souza, and M. Buongiorno Nardelli, Phys. Rev. B **69**, 035108 (2004).
[5] A. Aguado, L. Bernasconi, and P. A. Madden, J. Chem. Phys. **118**, 5704 (2003).
[6] C. Sagui, P. Pomorski, T. A. Darden, and C. Roland, J. Chem. Phys. **120**, 4530 (2004).
[7] P. Ordejón, E. Artacho, and J. M. Soler, Phys. Rev. B **53**, R10441 (1996).
[8] M. Schutz and H.-J. Werner, J. Chem. Phys. **114**, 661 (2001).
[9] A. J. Williamson, R. Q. Hood, and J. C. Grossman, Phys. Rev. Lett. **87**, 246406 (2001).
[10] P. Umari, G. Stenuit, and S. Baroni, Phys. Rev. B **79**, 201104 (2009).
[11] S. Curtarolo, G. L. W. Hart, M. Buongiorno Nardelli, N. Mingo, S. Sanvito, and O. Levy, Nat. Mater. **12**, 191 (2013).
[12] Editorial, Nat. Mater. **12**, 173 (2013).
[13] O. K. Andersen and T. Saha-Dasgupta, Phys. Rev. B **62**, R16219 (2000).
[14] N. Marzari, A. A. Mostofi, J. R. Yates, I. Souza, and D. Vanderbilt, Rev. Mod. Phys. **84**, 1419 (2012).
[15] W. C. Lu, C. Z. Wang, T. L. Chan, K. Ruedenberg, and K. M. Ho, Phys. Rev. B **70**, 041101 (2004).
[16] X. Qian, J. Li, L. Qi, C.-Z. Wang, T.-L. Chan, Y.-X. Yao, K.-M. Ho, and S. Yip, Phys. Rev. B **78**, 245112 (2008).
[17] I. Souza, N. Marzari, and D. Vanderbilt, Phys. Rev. B **65**, 035109 (2001).
[18] The PAOs are from publicly available files. Ω_1: [Ne], $3s^23p^2$, Si.pbe-n-rrkjus_psl.0.1.UPF. Ω_2: [Ne], $3s^23p^23d^0$, Si.pbe-n-rrkjus_psl.0.1.UPF. Ω_3: [core] $4s^24p^65s^14d^55p^0$, Mo.pbe-spn-rrkjus_psl.0.2.UPF. Ω_4: [core] $5d^{9.5}6s^16p^{0.5}$, Au.pbe-van_ak.UPF. Available at: http://www.quantum-espresso.org/?page_id=190.
[19] P. Giannozzi, S. Baroni, N. Bonini, M. Calandra, R. Car, C. Cavazzoni, D. Ceresoli, G. L. Chiarotti, M. Cococcioni, I. Dabo, A. Dal Corso, S. de Gironcoli, S. Fabris, G. Fratesi, R. Gebauer, U. Gerstmann, C. Gougoussis, A. Kokalj, M. Lazzeri, L. Martin-Samos, N. Marzari, F. Mauri, R. Mazzarello, S. Paolini, A. Pasquarello, L. Paulatto, C. Sbraccia, S. Scandolo, G. Sclauzero, A. P. Seitsonen, A. Smogunov, P. Umari, and R. M. Wentzcovitch, J. Phys.: Condens. Matter **21**, 395502 (2009).

[20]R. Dovesi, B. Civalleri, C. Roetti, V. R. Saunders, and R. Orlando, *Reviews in Computational Chemistry* (John Wiley & Sons, New York, 2005), pp. 1–125.
[21]L. A. Agapito and H.-P. Cheng, J. Phys. Chem. C **111**, 14266 (2007).
[22]Y.-S. Lee, M. Buongiorno Nardelli, and N. Marzari, Phys. Rev. Lett. **95**, 076804 (2005).
[23]P. S. Krstić, X.-G. Zhang, and W. H. Butler, Phys. Rev. B **66**, 205319 (2002).
[24]L. Agapito and M. Buongiorno Nardelli (unpublished).
[25]S. Curtarolo, W. Setyawan, S. Wang, J. Xue, K. Yang, R. H. Taylor, L. J. Nelson, G. L. W. Hart, S. Sanvito, M. Buongiorno Nardelli, N. Mingo, and O. Levy, Comput. Mater. Sci. **58**, 227 (2012).